

www.acsnano.org

Few-Layer MoS₂ Photodetector Arrays for Ultrasensitive On-Chip Enzymatic Colorimetric Analysis

Younggeun Park,**,* Byunghoon Ryu,* Seung Jun Ki, Brendan McCracken, Amanda Pennington, Kevin R. Ward, Xiaogan Liang,* and Katsuo Kurabayashi*



Cite This: ACS Nano 2021, 15, 7722–7734



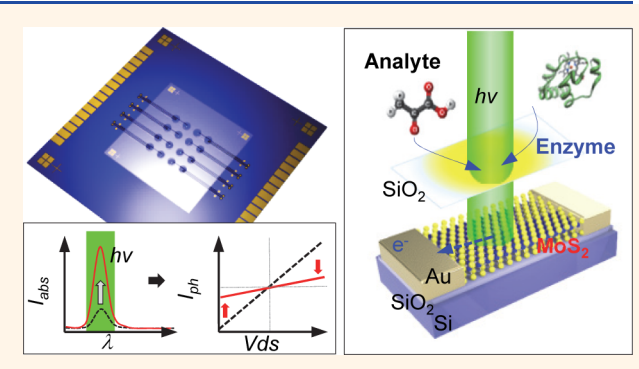
ACCESS I

Metrics & More

Article Recommendations

si Supporting Information

ABSTRACT: Enzymatic colorimetric analysis of metabolites provides signatures of energy conversion and biosynthesis associated with disease onsets and progressions. Miniaturized photodetectors based on emerging two-dimensional transition metal dichalcogenides (TMDCs) promise to advance point-of-care diagnosis employing highly sensitive enzymatic colorimetric detection. Reducing diagnosis costs requires a batched multisample assay. The construction of few-layer TMDC photodetector arrays with consistent performance is imperative to realize optical signal detection for a miniature batched multisample enzymatic colorimetric assay. However, few studies have promoted an optical reader with TMDC photodetector arrays for on-chip operation.



Here, we constructed 4×4 pixel arrays of miniaturized molybdenum disulfide (MoS₂) photodetectors and integrated them with microfluidic enzyme reaction chambers to create an optoelectronic biosensor chip device. The fabricated device allowed us to achieve arrayed on-chip enzymatic colorimetric detection of D-lactate, a blood biomarker signifying the bacterial translocation from the intestine, with a limit of detection that is 1000-fold smaller than the clinical baseline, a 10 min assay time, high selectivity, and reasonably small variability across the entire arrays. The enzyme $(Ez)/\text{MoS}_2$ optoelectronic biosensor unit consistently detected D-lactate in clinically important biofluids, such as saliva, urine, plasma, and serum of swine and humans with a wide detection range $(10^{-3}-10^{3}\,\mu\text{g/mL})$. Furthermore, the biosensor enabled us to show that high serum D-lactate levels are associated with the symptoms of systemic infection and inflammation. The lensless, optical waveguide-free device architecture should readily facilitate development of a monolithically integrated hand-held module for timely, cost-effective diagnosis of metabolic disorders in near-patient settings.

KEYWORDS: enzymatic colorimetric analysis, multiarray assay, MoS₂, photodetector array, point-of-care, D-lactate, metabolic acidosis

etabolomics work has identified biomarkers that can specifically distinguish different disease types, stages, progressions, and overall patient survival rates. 1,2 A promising strategy to determine disease presence and progression is to analyze specific changes of target metabolites in biofluids of the body.³⁻⁶ D-Lactate has gained much attention as an important metabolite biomarker due to its association with short bowel syndromes leading to severe metabolic acidosis, where overproduction of D-lactate causes neurological symptoms, including altered mental status, memory deficits, slurred speech, confusion, disorientation, abnormal gait, problems with muscle coordination, and even coma.⁷⁻¹¹ D-Lactate is produced by fermentative bacteria in the gastrointestinal tract, such as lactobacilli and bifidobacteria. 12 Plasma D-lactate is potentially an early predictor of septic shock and shown to be a promising biomarker of sepsis

as well as neonatal necrotizing enterocolitis due to reduced perfusion of the intestine, resulting in bacterial translocation. As such, rapid detection of D-lactate near the patient allows clinicians to intervene in life-threatening illnesses and metabolic disorders in a timely manner. Furthermore, lactates in the human body exist in both L- and D-isomeric forms, which are produced by different metabolic pathways. Compared to D-lactate, L-lactate is more abundantly

Received: February 15, 2021 Accepted: April 1, 2021 Published: April 7, 2021





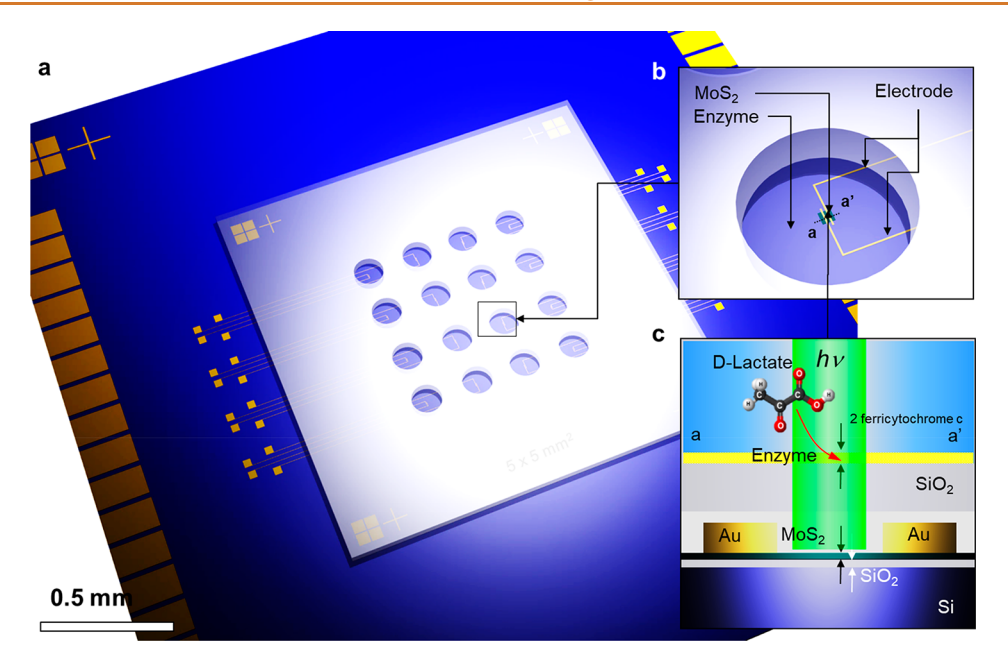


Figure 1. Device architecture for on-chip enzymatic colorimetric analysis. (a) Schematic of the integrated enzymatic colorimetric biosensor chip with 4×4 MoS₂ photodetector arrays (scale bar = 0.5 mm). (b) Single biosensor unit at each pixel. The unit has an integrated structure consisting of (i) a SiO₂ substrate supporting a PDMS microfluidic chamber whose bottom layer is optically transparent and covered with an immobilized enzyme film (Ez chamber substrate), (ii) an intermediate air gap, (iii) Au source and drain microelectrodes, and (iv) a SiO₂/Si substrate with a patterned few-layer 2D MoS₂ photodetector channel (optical reader substrate). The Ez chamber substrate is replaceable for repeated measurements of different samples. (c) Cross-section of the single biosensor unit in (b). The platform structures provided by the microelectrodes allow the air gap to be formed between the bottom of the Ez chamber substrate and the MoS₂ photodetector channel. The optoelectronic transduction does not require any special optical components (e.g., lens and waveguides) to feed the optical signal from the Ez chamber to the MoS₂ channel. The air gap provides a physical separation to block electrical interferences from the aqueous sample solution in the Ez chamber to the MoS₂ channel.

produced by the metabolic function of all normal mammalian cells. 15,16 The concentration of L-lactate in serum ($\sim\!100.0~\mu\mathrm{g/mL}$) is approximately 100 times higher than that of D-lactate (0.5–2 $\mu\mathrm{g/mL}$). 17 In testing a typical blood sample containing both isomers, selective detection of the time variation of low-abundant D-lactate is critical to monitor the progress of disease development. 7,8 In addition, continuous monitoring of the patient's D-lactate level would require a highly sensitive methodology that permits frequent assays by handling a small sample volume.

Traditional methods commonly used for lactate analysis include high-performance liquid chromatography (HPLC), 18 fluorometry, 19 magnetic resonance spectroscopy, 20 and enzymatic colorimetric analysis. 12,21,22 Although these methods provide quantitative results with high sensitivity, they are only suited for use in clinical laboratories, requiring complicated sample pretreatment, expensive machines, and trained human resources. Simplifying the optical setup for miniaturized pointof-care colorimetric analysis of D-lactate with a conventional approach would suffer from limited sensitivity and instrumental flexibility. In recent years, the research community has seen emerging approaches for rapidly monitoring low-abundance biomolecules, which employ nanobiosensing methods such as surface plasmon resonance, 23,24 surface-enhanced Raman scattering, ^{25,26} and plasmonic enzyme-linked immunosorbent assay. ^{27–29} However, these methods still require large-volume off-chip optical signal detection setups operated by means of complicated principles of physics and chemistry, and they also require long sample preparation steps especially for clinical sample tests. Atomically layered two-dimensional (2D) transition metal dichalcogenides (TMDCs), such as molybdenum disulfide (MoS_2), tungsten diselenide (WSe_2), and tungsten disulfide (WS_2), have recently garnered attention as promising photoconducting materials to create high-performance photodetectors and other relevant nanoelectronic devices. These 2D semiconducting devices possess nano- to microscale dimensions, superior electronic and optical properties, low power requirements, and compatibility with planar nanofabrication processes. Of particular note is that the charge transport characteristics of MoS_2 photoconducting channels are highly sensitive to optical stimuli with fast response speed and low internal electrical noise level, $^{33-35}$ which would be highly desirable to realize TMDC-based highperformance miniaturized colorimetric nanobiosensing.

Here, we demonstrate sensitive and rapid on-chip quantification of D-lactate using 4 × 4 arrays of ultrasensitive integrated photodetectors comprising MoS₂ photoconducting channels patterned beneath microfluidic reactor chambers. These microfluidic chambers have a bottom layer coated with an enzyme (Ez) film and serve as enzymatic reactor chambers (Ez chambers). According to the nanoplasmonic biosensor/ MoS₂ photodetector integration approach in our latest studies, \$6,37 the system architecture using an air gap between the reactor and the MoS₂ photodetector is designed to avoid electrical interference due to physical interaction between an aqueous biofluid and the active region of few-layer MoS₂ channels. A change in the transmission of illumination light through each Ez chamber is induced by colorimetric enzyme reaction and directly measured by the underlying MoS₂ photodetector pixel. The area size of the photodetector pixel is very small ($\sim 20 \times 20 \ \mu \text{m}^2$) as compared to that of the Ez chamber (750 μ m in radius). This feature eliminates the need

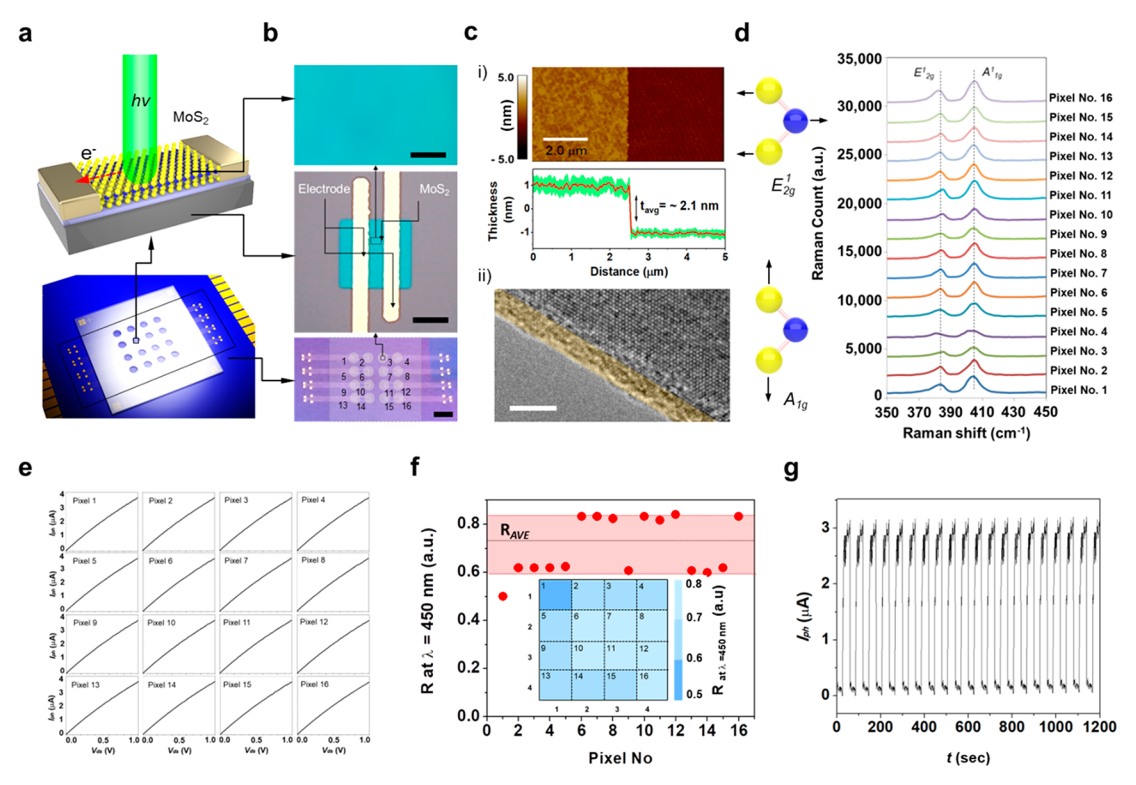


Figure 2. Few-layer MoS₂photodetector arrays and their optoelectronic characteristics. (a) Schematic of photoconduction in the MoS₂ photodetector pixel under light illumination at $\lambda=450$ nm. (b) Optical images of the MoS₂ layer deposited on the optical reader substrate (top; scale bar = 1 μ m), the MoS₂ photodetector pixel (middle; scale bar = 10 μ m), and the 4 × 4 Ez chamber arrays (bottom; scale bar = 800 μ m). The single-colored surface indicates the uniform thickness of the MoS₂ layer. (c) (i) Atomic force microscopy (AFM) image of one of the 4 × 4 MoS₂ photodetector channels patterned on the optical reader substrate (scale bar = 2 μ m); (ii) transmission electron microscopy (TEM) image for a representative synthesized MoS₂ sheet (scale bar = 2 nm). The colored region represents the cross-section of the sheet. (d) Raman spectrum of the 4 × 4 MoS₂ channels (16 pixels). (e) Drain-source current (I_{ds}) measured for the 4 × 4 MoS₂ channels as a function of drain voltage (V_{ds}) varying from 0 to 1 V under light illumination (λ = 450 nm and P = 0.5 mW). (f) Photoresponsivity of the 4 × 4 MoS₂ channels at λ = 450 nm and V_{ds} = 1 V. (g) Photocurrent (I_{ph}) response of the MoS₂ channel to repeated ON/OFF laser illumination (λ = 450 nm and P = 0.5 mW) cycles.

for stringent optical alignment and optical coupling with lenses or waveguides. Despite the simple, optical component-free integration scheme, our device is able to quantify D-lactate in a sample of 2.5 μ L with a sample-to-answer time of 10 min and a limit of detection (LOD) as small as $0.51 \times 10^{-3} \, \mu \text{g/mL}$, which is more than 1000 times lower than the clinical baseline, at a power consumption of 1-50 μ W. ³⁷⁻⁴⁰ In addition, the selective enzyme reaction in the Ez chamber allows our assay to distinguish D-lactate from its isomer, L-lactate, in a wide range of concentrations. We also have demonstrated that the integrated optoelectronic biosensor can yield comparable detection signals in saliva, urine, and serum of humans and swine. Further study with clinical human samples indicates that D-lactate can be a potential biomarker for sepsis. Our miniaturized Ez/MoS2 optoelectronic colorimetric biosensor platform could be further leveraged to serve as a diagnostic device with high-throughput testing and highly sensitive nanosensing capabilities for point-of-care disease screening and monitoring.

RESULTS AND DISCUSSION

Integrated Few-Layer MoS_2 Photodetector Arrays. Figure 1 illustrates the constructed 4 × 4 array-based Ez/MoS_2 optoelectronic biosensor chip device for analyzing D-lactate in multiple small-volume samples. The overall chip architecture includes a bottom SiO_2/Si substrate bearing a lithographically

fabricated MoS2 photodetector array (dubbed as optical reader substrate), an upper SiO2 layer (dubbed as Ez chamber substrate), and a reactor chamber array aligned to the photodetector array. The biosensor unit at each array pixel consists of a reactor chamber built on the Ez chamber substrate that is coated with an enzyme layer as well as a MoS₂ photodetector on the underlying optical reader substrate (Figure 1a and b). In the integrated device architecture, the chamber substrate and the optical reader substrate are assembled with an intermediate gap of air between them (Figure 1c). This air gap effectively prevents the shortcircuiting and electron transfer in MoS2 photoconducting channels caused by the redox reaction of a liquid-phased sample. As such, D-lactate oxidation by Ez (e.g., D-lactate dehydrogenases) is the only factor that triggers the photoelectric response in a MoS2 photodetector in response to the presence of D-lactate in the sample solution loaded to the Ez chamber. Here, the MoS₂ photodetector is sensitive to the optical stimuli at wavelengths ranging from 400 to 650 nm and suitable for D-lactate detection. The highly efficient charge separation and transport in the few-layer MoS₂ photoconducting channel yield the high sensitivity and fast response of the photodetector upon light illumination (Figure 2 and Figure 2a).⁴⁰

The details of the device fabrication process are presented in the Supporting Information (Figure S1). Briefly, we first

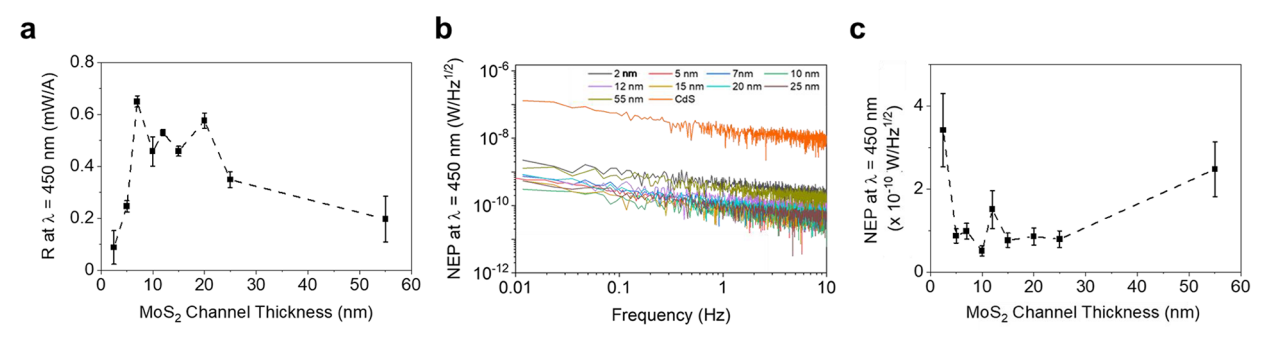


Figure 3. Photoresponse characteristics of the MoS₂ photodetectors with different MoS₂ thicknesses. (a) Photoresponsivity as a function of MoS₂ photoactive thickness measured at $V_{\rm ds}=0.4~{\rm V}$ under light illumination at $\lambda=450~{\rm nm}$ and $P=0.43~{\rm mW}$. (b) Noise equivalent power (NEP) spectra measured from MoS₂ devices with different thicknesses as well as a commercial CdS photodetector ($\sim1~\mu{\rm m}$ in layer thickness) for comparison. (c) NEP values captured at 1 Hz plotted as a function of MoS₂ thicknesses.

formed a 20 \times 20 mm² MoS₂ layer on the SiO₂/Si substrate through chemical vapor deposition (CVD)^{41,42} and patterned it into a 4 × 4 array of photodetection channels, each with a size of $\sim 20 \times 20 \ \mu \text{m}^2$. For construction of the arrayed MoS₂ devices, it was imperative to produce atomically layered MoS₂ sheets with a good uniformity over large areas. Photographs taken from as-fabricated MoS2 pixels exhibit uniform light blue color over the entire pixel array, which implies a good uniformity of these few-layer MoS₂ channels (Figure 2b). Next, we patterned a pair of 100 nm thick gold electrodes on both ends of each MoS2 channel, which serve as the source and drain contacts of the photodetector. The small channel size of \sim 2 μ m \times 20 μ m ensures that a single-crystalline structure is formed in each channel. Photoexcited carriers in the singlecrystalline channel between the source and drain contacts are expected to experience no grain boundary scattering, thus providing an excellent photoresponse property and noise characteristics for the MoS₂ photodetector. Meanwhile, we prepared a 300 μ m thick SiO₂ layer that eventually served as the supporting structure for all Ez chambers after the whole device assembly. The surface of this SiO₂ layer was coated with a film of D-lactate dehydrogenase, or D-LDH (see Methods). We also took a photograph of a $\sim 25 \text{ mm}^2$ area of the enzyme film formed on the SiO₂ substrate and observed its uniform color, by which we confirmed a uniform distribution of the enzyme on the SiO₂ supporting surface. Subsequently, the prepared SiO₂ supporting layer was placed on top of the gold electrodes, and the uncovered electrode areas were used to provide access for electrical wiring. Finally, we fabricated the chamber wells of 750 μ m in radius within a polydimethylsiloxane (PDMS) layer and attached the layer onto the SiO₂ supporting substrate using alignment marks to create the Ez chamber substrate. The Ez chamber substrate was designed to be disposable for each detection, but the underlying MoS₂ photodetector array can be repeatedly exploited for multiple measurements.

Before assembling the whole device chip, we took atomic force microscopy (AFM) images of the 4×4 MoS $_2$ channels patterned on an optical reader substrate to additionally quantify their thickness uniformity (Figure 2c). The average thickness of the MoS $_2$ channels was measured to be 2.1 nm with a standard variance of <10% over the whole array (Figure S2). We also acquired a transmission electron microscopy (TEM) image for a representative synthesized MoS $_2$ sheet (Figure 2c) and the Raman spectra from the 4×4 MoS $_2$ channel pixels and observed two characteristic peaks consistently at 384 and 407 cm $^{-1}$ for each pixel (Figure 2d).

These characteristic peaks are associated with the E^1_{2g} and A^1_{g} modes of MoS₂ layers, respectively. The E^1_{2g} mode reveals the in-plane motion of Mo and S atoms, whereas the A_{1g} mode is attributed to the out-of-plane vibration of Mo and S. These Raman peaks and the TEM image indicate that the thickness values of the MoS₂ channels are around three or four atomic layers, consistent with previously reported thickness measurements. 42,43

After the whole device chip was fabricated, we characterized the optoelectronic performance of the MoS₂ photodetectors using an experimental setup including a probe station, a semiconductor analyzer, and a 0.5 mW laser as an illumination source at $\lambda = 450 \pm 10$ nm (see Methods and Figure S3). The maximum absorption spectrum of the enzyme reaction was found to exist at this light wavelength. We measured the drain-source current (I_{ds}) as a function of drain voltage (V_{ds}) for all 4 × 4 MoS₂ photodetectors and observed consistent transport characteristics among them (Figure 2e). We subsequently confirmed the uniformity of the optoelectronic characteristics for all 4×4 MoS₂ photodetectors in an array by measuring the photoresponsivity and photocurrent of each photodetector (Figure 2f and Figure S4). For each photodetector, we observed a strong and consistent photoresponsivity at the wavelength window of $\lambda = 400-500$ nm, which is desirable for the assay based on light absorption variations accompanying the enzyme reaction. The coefficient of variation (CV) in photoresponsivity at $\lambda = 450$ nm across the whole $4 \times 4 \text{ MoS}_2$ photodetector array was determined to be <11.5%. We further confirmed the consistent photoresponses of the 4 × 4 MoS₂ photodetectors by measuring their photocurrents $(I_{ph} = I_{ds_light} - I_{ds_dark})$ under repeated ON (30 s) and OFF (30 s) illumination cycles at $\lambda = 450$ nm (Figure 2g). For a typical photodetector, once the illumination is ON, $I_{\rm ph}$ rapidly increases from ~0 to 3.3 μ A. The average dark current of the MoS₂ photodetectors is at \sim 0.5 nA \pm 2%. The typical power consumption of these MoS₂ photodetectors was as small as $1-50 \mu W$. Thus, the optical reader of our device chip exhibits high power efficiency. Additionally, we characterized the photoresponse property for an as-fabricated MoS₂ photodetector and the same device after 9 months of storage in ambient conditions and obtained similar external quantum efficiency (EQE) data in both cases (Figure S5). The MoS₂ device manifests excellent long-term stability and reproducibility as reported in our previous study.⁴⁴

Thickness Effect on MoS₂ Photodetectors' Optoelectronic Performance. The MoS₂ thickness could affect the photoresponse and noise characteristics of the MoS₂ photo-

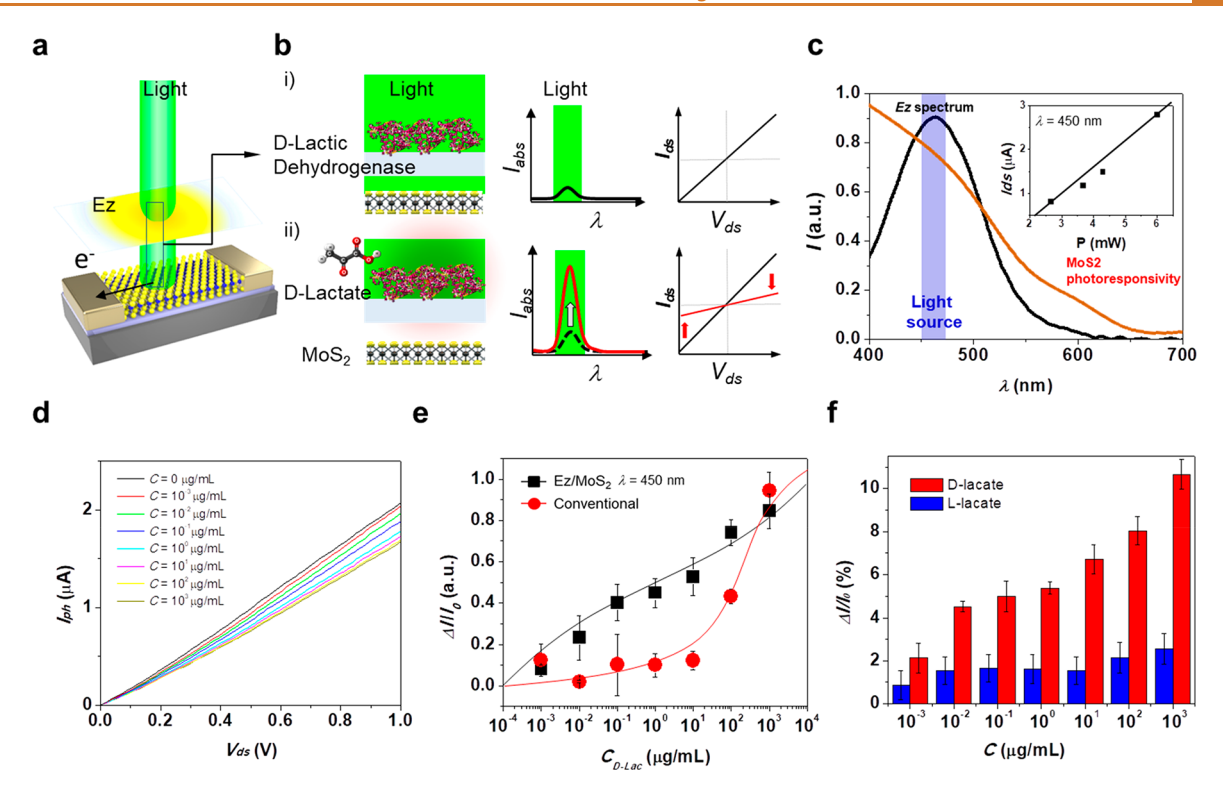


Figure 4. Results of the on-chip D-lactate enzymatic colorimetric assay using the integrated Ez/MoS_2 optoelectronic biosensor unit. (a) Schematic of the enzyme film and MoS_2 photodetector channel of a single biosensor unit under light illumination. The enzyme reaction on the enzyme film determines the light transmission to the MoS_2 photodetector. (b) Detection mechanism of the integrated Ez/MoS_2 optoelectronic biosensor unit. The reaction between D-lactate and ferricytochrome c that is catalyzed by the enzyme (D-LDH) changes the optical density (OD) of the solution in the Ez chamber at λ = 450 nm. The degree of the OD change depends on the D-lactate concentration, CD-Lac, which determines the intensity of light transmitted to the underlying MoS_2 photodetector channel. Accordingly, the drain—source current of the channel I_{ds} varies with CD-Lac. Therefore, measuring I_{ds} enables the quantification of CD-Lac. (c) Absorption spectrum of the solution experiencing the D-lactate enzyme reaction (black) and photoresponsivity spectrum of the MoS_2 photodetector channel (red). They are compared to the emission spectral window of the light source (λ = 450 nm \pm 10%). (d) Photocurrent, I_{ph} , of the MoS_2 photodetector at CD-Lac = $10^{-4} \rightarrow 10^3 \,\mu\text{g/mL}$ at λ = 450 nm and P = 0.5 mW. (e) Standard calibration curve of the on-chip D-lactate enzymatic colorimetric assay using the integrated Ez/MoS_2 optoelectronic biosensor unit at λ = 450 nm and P = 0.5 mW. (f) Bar chart of the biosensor signal, which is the normalized photocurrent $\Delta I/I_{0}$, for PBS solutions spiked with D-lactate and L-lactate at various concentrations. Error bars represent the standard deviation errors (n = 5, P < 0.05).

detector and therefore be critical for the detection limit of the integrative biosensor. To study the effects of the MoS₂ thickness on the photoresponse characteristics of MoS₂ photodetectors, we fabricated a set of photodetectors with different MoS2 channel thicknesses ranging from ~2 to 55 nm (Methods). The photocurrents ($I_{\rm ph} = I_{\rm ds_light} - I_{\rm ds_dark}$) of these devices were measured under the illumination of a 450 nm laser and channel bias $V_{\rm ds}$ of 0.4 V. Figure 3(a) shows the responsivity ($R = I_{ph}/P_{light}$) data measured from these devices that are plotted as a function of their MoS2 thicknesses. The data show that photoresponsivity first increases with increasing MoS₂ thickness from 2.5 to 7 nm. This can be attributed to the net effect of two possible reasons. First, the increase in the MoS₂ photoactive layer thickness is expected to enhance the total amount of photogenerated carriers under a given illumination condition, therefore resulting in a higher photocurrent. Second, this increase is also expected to result in a smaller fraction of photogenerated carriers that are subjected to the recombination sites associated with the dangling bonds or interfacial defects on the SiO₂ substrate. Figure 3(a) also indicates that 7-20 nm thick MoS₂ photoactive layers result in relatively higher and constant photoresponsivity values. The photoresponsivity gradually decreases with the MoS₂ thickness further increasing beyond 20 nm. This is

attributed to the limited penetration depth of visual light into the MoS_2 layers, resulting in poor efficiency of collecting photogenerated carriers. Experimental observations demonstrated that the skin depth of the MoS_2 photodetector is ~ 5 nm at a peak frequency of ~ 3 eV. Thus, the further increase of MoS_2 thickness over 7 nm does not enhance the photocurrent but adversely increases the dark current. Our result is in good agreement with previous studies with discrepancies arising from the difference in laser wavelength and fabrication methods.

We further investigated the effects of the MoS_2 thickness on the noise characteristics of MoS_2 photodetectors. Specifically, the low-frequency (0.1-10~Hz) noise fluctuations in the photocurrent signals were measured from the photodetectors with various MoS_2 thicknesses under the illumination condition. The measurement details are described in the Methods section. Figure 3(b) displays the noise spectra measured from a set of MoS_2 photodetectors. Our devices exhibit a typical 1/f noise characteristic, which is associated with imperfect ohmic contacts, dangling bonds at material interfaces, and charge trapping/detrapping events. For the photodetector, noise equivalent power (NEP), defined as noise spectral density divided by the responsivity, is usually used as an appropriate parameter to evaluate the detection sensitivity

of photodetectors. 50 Figure 3(b) shows the NEP spectra of all devices. From these spectra, the NEP values at 1 Hz are acquired and plotted as a function of MoS2 thicknesses in Figure 3(c). Here, the NEP data at 1 Hz are specifically chosen for comparison because the time-dependent biosensing signals associated with binding reaction events typically take place in a time scale of several seconds, and therefore the noise fluctuations around 1 Hz are expected to be the most critical for determining the signal-to-noise ratio. Figure 3(c) shows that the devices with MoS₂ thickness in the range of 7-25 nm exhibit the lowest NEP values, which are anticipated to lead to higher detection sensitivity for optoelectronic biosensors. For the devices with MoS₂ thickness > 25 nm, their relatively larger NEP values are attributed to the gradual decrease of photoresponsivity, as already shown in Figure 3(a). For the devices with MoS₂ thickness < 7 nm, their relatively larger NEP values are attributed to the more prominent scattering effects between photogenerated carriers and dangling bonds or traps at MoS₂/SiO₂ interfaces, charge impurities, and lower responsivity level in comparison with the devices with thicker MoS₂ layers. 51,52 Here, it should be noted that the NEP values of all MoS₂ photodetectors are significantly lower than that measured from a commercial CdS photodetector, as shown in Figure 3(c). Therefore, the photodetectors with a MoS₂ thickness of ~2 nm, although not the optimal thickness, are still advantageous over conventional photodetectors in terms of NEP characteristics. Besides, MoS2 films with a thickness of ~2 nm can be efficiently produced using CVD, suitable for making MoS₂ photodetector arrays, whereas the present convenient approaches capable of generating MoS2 samples thicker than 10 nm are based on exfoliation methods, not suitable for large-area implementations. Considering such a trade-off between NEP performance and viability for large-area implementation, we decided to use the ~2 nm thick MoS₂ photoactive channels fabricated above.

High-Performance D-Lactate Detection with an Integrated Ez/MoS₂ Biosensor Pixel. Using the biosensor unit at pixel #7 (see inset of Figure 2f) on the aforementioned device chip, we performed on-chip enzymatic colorimetric analysis of D-lactate (Figure 4). The detection principle involved measurement of the enzyme-reaction-induced optical transmission change as a function of D-lactate concentration with the underlying MoS₂ photodetector (Figure 4a). Specifically, in the Ez chamber, the enzyme, D-LDH, selectively catalyzed the reaction of D-lactate with its substrate molecule (ferricytochrome c) (Figure 4b and Figure S6). In the absence of D-lactate, the incident light at $\lambda = 450$ nm passed through the buffer solution in the chamber with the highest transmission, which resulted in maximum photoconduction in the MoS₂ channel on the underlying optical reader substrate. Loading a D-lactate-containing solution mixed with ferricytochrome c onto the Ez chamber resulted in the oxidation of Dlactate. It increased the absorbance of the solution and translated into decreased photoconduction in the MoS₂ channel. Correlating the measured photoconduction variation with the D-lactate concentration permitted highly sensitive colorimetric analyte quantification.

The MoS₂ photoconducting channel under measurement showed a high photoresponsivity at the operating wavelength of $\lambda = 450$ nm (Figure 4c). This conveniently overlapped with the aforementioned absorption spectrum peak of the enzyme reaction whose value varies with the D-lactate concentration (Figure S6) and enabled highly sensitive detection of D-lactate.

The photoresponse behavior of the integrated optoelectronic biosensor device was further characterized at different D-lactate concentrations (Figure 4d and Figure S8). Here, we loaded a phosphate-buffered saline (PBS) solution spiked with D-lactate of known concentration onto the Ez chamber and incubated the solution for 10 min under dark conditions. The baseline dark current was observed to be highly stable at $I_{ds,dark} \approx 0.5$ nA. After a 10 min incubation period, we turned on the illumination light and measured the photocurrent I_{ph} , which took 1 s. After performing the assay with a sample at a particular D-lactate concentration (CD-Lac), we replaced the Ez chamber substrate with another one for the next measurement at another concentration. The measured value of $I_{\rm ph}$ at $V_{\rm ds}=1$ V was 1.6 μ A for CD-Lac = 100 μ g/mL, and it approximately linearly decreased from $\sim 2.1 \mu A$ to $\sim 1.55 \mu A$ with CD-Lac varied from 10^{-3} to $10^{3}\mu g/mL$. From this measurement, we obtained a sensor calibration curve plotting the normalized photocurrent change $\Delta I_{\rm ph}/I_{\rm ph0}$ as a function of CD-Lac (Figure 4(e)). The calibration curve of the pixel #7 biosensor unit showed a wide (6-log) dynamic range of detection from 10⁻³ to $10^3 \mu g/mL$. The LOD (LOD_{Ez/MoS2}) of the Ez/MoS₂ biosensor unit at pixel #7 was estimated to be 0.51×10^{-3} μ g/mL. Here, the LOD_{Ez/MoS2} value was estimated using LOD = $3\sigma/k_{\rm slope}$, where σ and $k_{\rm slope}$ are the standard deviation of the background signal measured from a blank control and the regression slope of the calibration curve, respectively. Meanwhile, we additionally performed a colorimetric enzymatic analysis for the same spiked PBS samples using a commercial microplate reader (Synergy Neo2 hybrid multi-mode reader, BioTEK). The dynamic range was determined to be between 10^{-1} and $10^3~\mu g/mL$ and the LOD (LOD_{col}) to be ~0.2 × $10^{-1}~\mu g/mL$, which is 100-fold larger than LOD_{Ez/MoS2}. The calibration curve of our on-chip colorimetric assay showed a much higher linearity and sensitivity for the concentration range of CD-Lac = 10^{0} – 10^{3} $\mu g/m$. Furthermore, $\Delta I_{\rm ph}/I_{\rm ph0}$ as a function of the air gap distance showed a minimal change (Figure S9). Here, the incident laser light is nearly collimated. The interrogation area of the EZ chamber (1500 μ m in diameter) is more than 40 000 times larger the area size of the MoS₂ photodetector channel ($\sim 2 \mu m \times 20 \mu m$). As such, any sub-millimeter-scale variation in the air gap distance yields a negligible geometrical change in the optical path of the light reaching the MoS₂ photodetector, and it does not alter much the light signal intensity detected by the MoS₂ photodetector. Thus, the Ez/MoS₂ biosensor yields consistent and sensitive Dlactate detection performance regardless of the variation in the air gap distance.

D- and L-Lactate are isomers, which are compounds with the same chemical formula, but with a different atomic arrangement on the molecule. As a result, these compounds possess different chemical properties. L-Lactate is mainly related to the metabolic status of the human body, and the production concentration of L-lactate in the body is usually 10-100 times higher than that of D-lactate. Owing to the high concentration of L-lactate endogenously found in the body, the detection of D-lactate is challenging. Here, we tested the selectivity of our chosen pixel unit to D-lactate by measuring $\Delta I_{\rm ph}/I_{\rm ph0}$ for both D-lactate and L-lactate in PBS (Figure 4f). Using the same device, no significant signal change was observed for the solution spiked with L-lactate regardless of the concentration, whereas the signal linearly increased with the concentration for the D-lactate-spiked solution. Thus, the cross-reactivity between the enzyme and L-lactate in the Ez chamber was

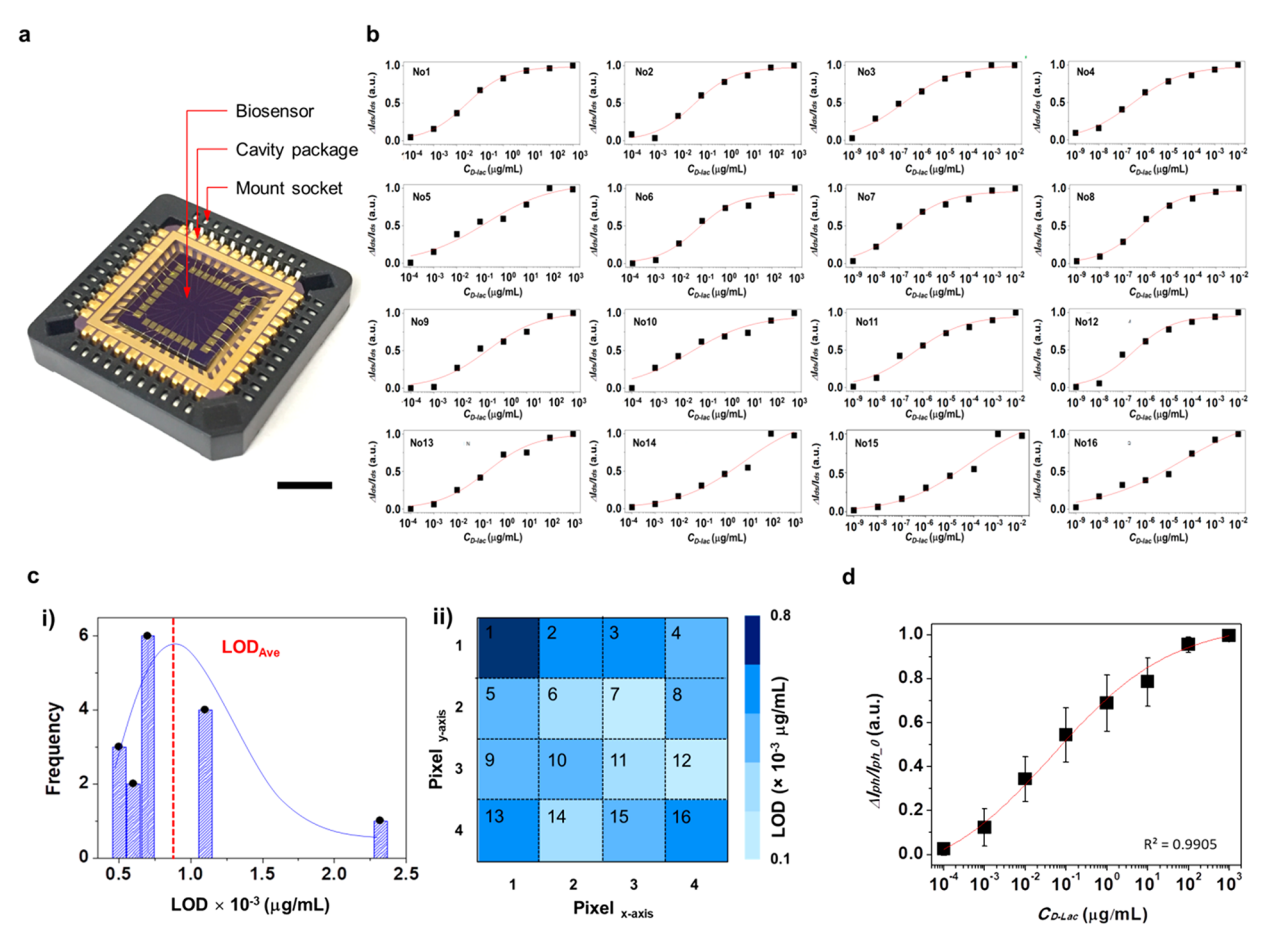


Figure 5. Performance distribution of 4×4 Ez/MoS_2 optoelectronic biosensor arrays for the on-chip D-lactate enzymatic colorimetric assay. (a) Optical image of the packaging of the integrated enzymatic colorimetric biosensor chip (scale bar = 1 cm). (b) Sixteen individual standard calibration curves obtained for the 4×4 Ez/MoS_2 optoelectronic biosensor arrays. (c) LOD distribution of the on-chip enzymatic colorimetry assays using the 4×4 Ez/MoS_2 optoelectronic biosensor arrays. The LOD values were obtained from the results measured from the 16 individual Ez chambers. The data show that these on-chip assays are 100 times more sensitive than the conventional colorimetric assay. (d) Calibration curve averaged over the data taken for the 16 standard calibration curves in (b). The CV of the signal distribution among the 4×4 biosensor arrays at each concentration lies between 5% and 18%.

negligible, and the Ez/MoS₂ biosensor unit was found to be highly selective to D-lactate at a wide range of concentrations.

Additionally, we examined the change of enzymatic activity over time and its impact on the long-term stability of our test using the biosensor (Figure S10). Several PDMS Ez chamber layers of the biosensor were stored at 4 °C after immobilizing the enzyme (D-LDH) and loading the substrate (ferricytochrome c) solution onto their Ez chamber arrays for t = 1month and 2 months. Meanwhile, we stored a solution mixture of D-LDH and ferricytochrome c in a PCR tube at 4 °C for the same period as above. At each time point, we measured the photocurrent signal $\Delta I/I_0$ of the biosensor with one of those PDMS Ez chamber layers integrated with the MoS₂ photodetector arrays (Figure S10a) and the signal of a plate-readerbased D-lactate assay using the stored enzyme/substrate mixture (Figure S10b) for D-lactate spike-in samples at four different concentrations. Accompanying the decline in enzymatic activity, we observed a sensor signal decrease by \sim 30% and \sim 50% at t=1 month and 2 months, respectively. This warrants the need for sensor calibration before each measurement or a better enzyme preservation protocol for poststorage future use.

Multisample Analysis Performance of the Arrayed Ez/ MoS₂ Optoelectronic Biosensors. To evaluate the overall multisample performance of the entire chip device, we repeated the aforementioned assay test for all of the 4×4 Ez/MoS₂ biosensors in an array (Figure 5). Figure 4a shows an as-fabricated 4×4 device array on a SiO₂/Si optical reader substrate, which was placed onto a cavity package in a mount socket using surface mounting technology (see Methods). We obtained the standard calibration curves for all 4 × 4 biosensors in the array by loading multiple samples (2.5 μ L each) onto 16 Ez chambers (Figure 5b). These curves showed highly consistent detection characteristics among these arrayed sensors for CD-Lac ranging from 10^{-3} to $10^{3} \mu g/mL$ under the same assay conditions involving a 10 min incubation. Analyzing the pixel-to-pixel LOD value distribution yielded a mean LOD value of $0.87 \times 10^{-3} \mu g/mL$ with a relative standard variance of 5% over the 4 × 4 biosensor array (Figure 5c). The minimal and maximal LOD values were found at pixel #7 (0.51 × 10⁻³ μ g/mL) and pixel #1 (2.32 × 10⁻³ μ g/mL), respectively. The outlier performance that pixel #1 shows could be attributed to local damage or contamination induced by the device fabrication process.

Even such a maximal LOD value is \sim 50 times lower than that obtained from conventional colorimetric detection methods. Figure 5d shows the overall standard curve obtained from the sensor response data averaged over all 4 \times 4

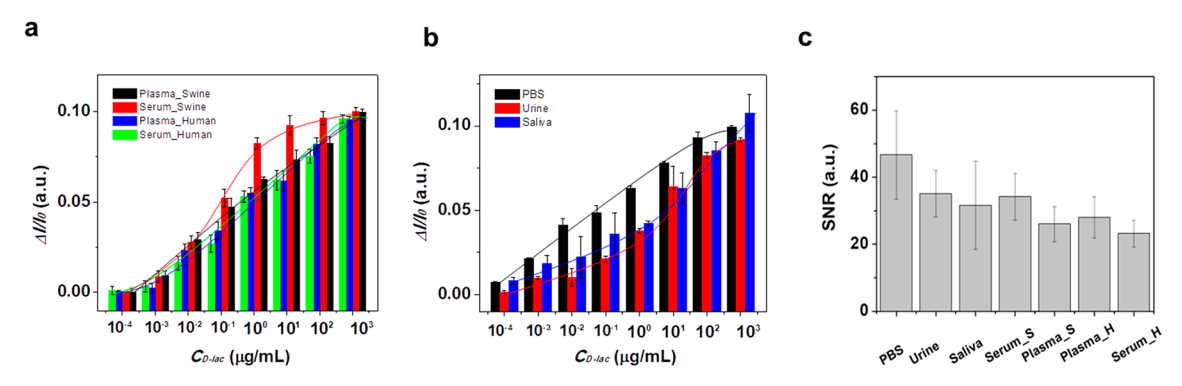


Figure 6. On-chip enzymatic colorimetric assay characteristics with clinically relevant biofluids. (a) Comparison of the calibration curves for D-lactate spiked in plasma and serum of swine and humans from healthy donors. (b) Comparison of the calibration curves for D-lactate spiked in urine and saliva, which are both relevant to a noninvasive, sample-preparation-free clinical test. (c) SNRs estimated for different clinically relevant biofluids spiked with D-lactate of 1 μ g/mL. The values followed one-way analysis of variance, which hypothesizes that SNR values are statistically identical across PBS, saliva, urine, plasma, and serum (P = 0.05 and P = 5).

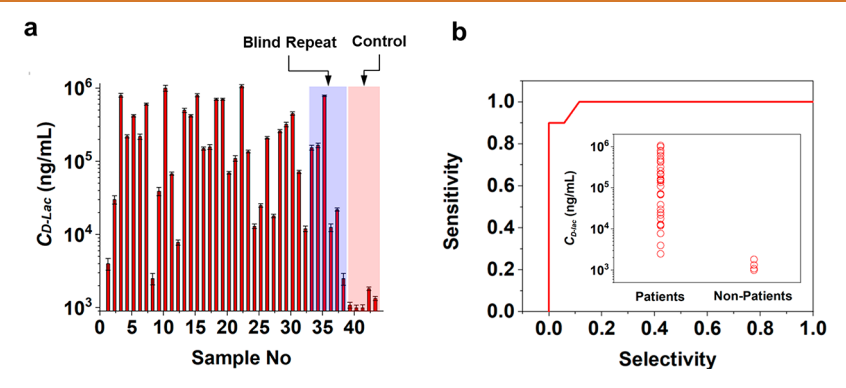


Figure 7. Serum sample detection using the integrated enzymatic colorimetric biosensor chip. (a) Quantified D-lactate levels of patients experiencing sepsis (n = 43). The study includes blind repeats of testing sample nos. 16, 17, 15, 35, 25, and 8 and control tests using healthy donor samples. (b) Receiver operating characteristic curve (ROC). The estimated area under the ROC curve (AUC) was 0.98. The threshold for both sensitivity and specificity was CD-Lac = 0.05 ng/mL. The inset plot shows D-lactate levels between sepsis patients and nonpatients (healthy subjects) (P < 0.0001).

biosensors in the array. The error bar associated with each data point represents the accuracy of the sensor signal output at its corresponding CD-Lac value. The data allow us to calculate the coefficient of variation of the signal output distribution across the entire array to be between 5% (minimum) and 18% (maximum) for the tested CD-Lac values between 10^{-4} and 10^{3} $\mu \rm g/mL$. The pixel-to-pixel performance variations likely stem from the variations in the photoresponsivity and $I_{\rm ds}{-}V_{\rm ds}$ characteristics among the sensing units in the array under test.

Clinically Relevant Biofluid Sample Analysis. Using the integrated $Ez/{\rm MoS}_2$ biosensor units, we performed the on-chip enzymatic colorimetric analysis of D-lactate in clinically relevant biofluids (Figure 6) under preclinical (animal) and clinical (human) conditions approved by respective institutional review boards of the University of Michigan. We first obtained the standard calibration curves for 2.5 μ L samples of plasma and serum from healthy swine and human donors that were spiked with D-lactate of known concentration. The calibration data obtained for both swine and human plasma were fitted to a regression curve with $R^2_{\rm swine\ plasma}=0.9453$ and $R^2_{\rm human\ plasma}=0.9876$, respectively. The LOD values estimated for swine and human plasm are LOD swine plasma $\approx 1.3 \times 10^{-3}$ μ g/mL and LOD human plasma $\approx 3.1 \times 10^{-3}$ μ g/mL, respectively (Figure 6a). In comparison, the literature 47 reports that plasma D-lactate quantification by the conventional colorimetric

analysis method yielded a LOD $\approx 100 \times 10^{-3} \ \mu \text{g/mL}$ and required a larger volume of 100 μ L for reliable detection.

In the clinical D-lactate analysis, most current methods involve the collection and purification of whole blood to extract plasma or serum, thus requiring additional time and labor. Furthermore, blood draw involves skin-piercing, which is often invasive and highly inconvenient to implement frequently. Clinical testing using urine or saliva is attractive, as it is noninvasive and sample-preparation-free. However, Dlactate concentrations in these fluids are extremely low. 7,8,11 Urine- or saliva-based D-lactate analysis necessitates a highly sensitive detection technique. We obtained the standard curve for saliva (simulated one) with $R^2_{\text{saliva}} = 0.9453$ at CD-Lac ranging from 10^{-3} to $10^3 \,\mu\text{g/mL}$ and determined the LOD_{saliva} to be $1.2 \times 10^{-3} \ \mu \text{g/mL}$. In contrast, the standard curve obtained for urine (simulated one) showed a less linear shape with $R^2_{\text{urine}} = 0.9712$ and yielded a two times higher LOD_{urine} of $2.7 \times 10^{-3} \,\mu\text{g/mL}$. We believe that such a lower sensitivity is attributed to the optical interference resulting from the higher light absorbance in urine at $\lambda = 450$ nm. Nonetheless, the results suggest that clinical testing with saliva and urine could be feasible with our device for its superior sensitivity. The obtained LOD is still 1000 times smaller than the clinical baseline of D-lactate in urine.8 We observed that the D-lactate calibration curves measured from urine and saliva samples are similar to that from the serum sample (Figure 6b). Furthermore, we measured the background and sensor signals at CD-Lac = 1 μ g/mL from PBS, saliva, urine, swine plasma, and human serum samples and compared the signal-to-noise ratios (SNRs) from these different media. Here, the SNR value was calculated as the signal divided by three times the standard deviation of the blank signal. The SNR from PBS (SNR_{PBS}) took the highest value of 46, whereas the values from other media are between 25 and 35. For example, SNR_{Saliva} and SNR_{Plasma} from the human samples were 30 and 29.5, respectively. With these results, we expect that the effect of the background on clinical test could be small. However, it should be noted that potential interferences due to abundant background enzymes still need be considered for a test using real saliva.

Subsequently, we performed clinical tests using the Ez/MoS_2 optoelectronic biosensor (Figure 7). We collected serum samples from patients with symptoms of systemic infection, inflammation, or both. We obtained 32 samples from septic patients and another five from healthy patients. We repeated the measurements for six samples blindly selected among the 32 tested samples and confirmed good reproducibility of our tests using the biosensor. Overall, we observed distinctly higher D-lactate levels for septic patient samples (Figure 7a). The range of the measured CD-Lac from sepsis patients is between 3×10^3 and 10^6 ng/mL, meanwhile the healthy human sample shows CD-Lac < 103 ng/mL (Figure 7b). The detected Dlactate level from the sepsis patients has a wide range. We next constructed a receiver operating characteristic (ROC) curve using the D-lactate level as a predictor. The optimal D-lactate cutoff that maximizes both sensitivity and specificity was 0.045 ng/mL. With this cutoff, the detection accuracy was 86.0%, the sensitivity 91.3%, and the specificity 82.4%. We applied the cross validation method to estimate the area under the curve (AUC). The AUC value for D-lactate as a sepsis biomarker was 0.98 (95% confidence interval). This value indicates the presence of a large patient-to-patient heterogeneity for sepsis.

CONCLUSION

Overgrowth of bacteria in colon or ischemic or damaged bowel is associated with an elevated concentration of D-lactate in the blood circulation. Excessive accumulation of D-lactate in the body due to D-lactate-producing bacteria can cause severe neurologic impairment. Its presence in the setting of possible infection may also signify sepsis in adults as well as the potential for necrotizing enterocolitis in neonates. Timely interventions of the D-lactate-caused neurotoxic disorders or the rapid diagnosis and treatment of sepsis and enterocolitis may require a miniaturized point-of-care diagnostic platform enabling rapid and sensitive near-patient detection of D-lactate. In this study, we successfully demonstrated a sensitive and selective on-chip enzymatic colorimetric analysis of D-lactate toward point-of-care diagnosis using a biosensor chip device. Our proof-of-concept device incorporated 4 × 4 arrays of integrated Ez/MoS2 optoelectronic biosensor units, all of which showed D-lactate detection performance with an acceptable level of pixel-to-pixel variability (CV = 5-18%) for a wide range of concentrations from 10^{-3} to $10^3 \,\mu\text{g/mL}$. The biosensor pixels of the device permitted D-lactate analysis in a biofluid sample of 2.5 µL with an average LOD value of $0.87 \pm 0.032 \times 10^{-3} \,\mu\text{g/mL}$ and a 10 min assay turnaround. Furthermore, the analysis distinguished D-lactate from L-lactate in a wide range of concentrations. Using the device, we additionally showed the ability to detect D-lactate at low

concentrations in urine and saliva as well as in plasma and serum. The urine- or saliva-based measurement would provide a noninvasive, sample-preparation-free clinical D-lactate test.

Over the last several years, significant research efforts have been undertaken to advance detection capabilities for lab-on-achip systems. Optical techniques that have been employed for point-of-care diagnostics include portable optical imaging systems and optical microscopes integrated to cell phones.⁵ For example, the hand-held plasmonic biosensor developed by Ozcan⁵⁴ is a good benchmark device, as it incorporates lensfree computational imaging using a commercial CMOS detector integrated into a highly compact hand-held platform. The device enables high-throughput and multiplexed label-free plasmonic biosensing detection. However, like other point-ofcare optical detection methods, the platform suffers from a lack of sensitivity resulting in a 1000 times larger LOD than a commercial plate-reader-based ELISA assay. In contrast, our 2D MoS₂ photodetector-based D-lactate assay provides a 100fold LOD compared with an assay using a commercial plate reader, thus clearly demonstrating superior sensitivity for point-of-care detection.

A key design feature of our on-chip enzymatic colorimetric platform is the air gap-mediated physical isolation of an aqueous solution in the microfluidic reactor chamber from the MoS₂ photodetectors on the optical reader substrate. This brings two advantages to the device operation. First, any undesirable electrical interferences can be prevented between the aqueous sample and the active MoS₂ channels. Second, the substrate holding the reactor chambers (*Ez* chamber substrate) is disposable and replaceable after each test to repeatedly use the optical reader substrate, which saves the hardware cost. Another important design feature is the simple optics arrangement not requiring strict optical alignment or waveguide coupling between the reactor chamber and the MoS₂ photodetector. This enabled us to create the whole platform with the easy and low-cost device integration and assembly strategy and to handle the repeated assays that involved many replacements of the Ez chamber substrate with no difficulty. A further scale-up of the on-chip integration of the arrayed biosensor structure by advancing our MoS2 array manufacturing and integration capabilities is needed to achieve higher assay throughput. A study is currently underway to achieve large-area manufacturing of a highly uniform single-crystal MoS₂ film on a substrate as the next step for the scale-up of the biosensor. The high-throughput biosensor could be implemented in an on-chip 96-well plate-like batched enzymatic colorimetric metabolite measurement near the patient, thus facilitating diagnosing neurotoxicity caused by D-lactate acidosis and monitoring the outcome of interventions in resource-limited and field-deployable settings with a short assay time, high sensitivity, and reduced diagnosis costs per patient.

METHODS

Chemicals. We obtained sulfur powders (S, 99.95%), molybdenum trioxide (MoO₃, 99.97%), APTES (99%), sodium D-/L-lactate (\geq 99% and \geq 98%), D-LDH (the purified product at a concentration of 10 mg/mL has an absorbance of 14.9 at λ = 280 nm), L-lactic acid (98%), L-ascorbic acid (99%), sodium sulfate (99%), sodium chloride (99%), calcium chloride (97%), potassium chloride (99%), citric acid (99.5%), potassium thiocyanate (99%), ammonium chloride (99.5%), potassium monobasic (99%), potassium dibasic (98%), and bovine serum albumin (98%) from Sigma-Aldrich (St. Louis, MO, USA) and used them without further purification or modification. We purchased

the 182 SIL ELAST KIT .5KG, including a PDMS elastomer and a curing agent, from Corning. Nanopure deionized (DI) water (18.1 $\mathrm{M}\Omega\text{-cm}$) was produced in-house.

 MoS_2 Synthesis. To obtain large-area MoS_2 (2 cm × 2 cm) with high uniformity, we synthesized the few-layer MoS2 sheet based on the CVD method. The SiO₂/Si substrates were first cleaned by using a piranha solution for 10 min and rinsed using DI water for 10 min. For the CVD process, we used a tubular furnace. For the MoS2 growth, 100 mg of S and 10 mg of MoO₃ powders were precisely weighed by using a microbalance and used as precursors. A sulfur powder boat was placed upstream, 20 cm away from the center of a 1 in. diameter quartz tube. A MoO₃ powder boat was located at the center of the tube, and the SiO₂/Si substrate was flipped and loaded onto the MoO₃ boat. We used Ar gas (99.999%, Cryogenic Gases) to deliver precursor molecules to the substrate at a flow rate of 150 sccm. After securing the sample and the inner gas flow in the tube, we turned on the heater from room temperature to 800 °C with a ramping rate of 20 °C. We conducted the synthesis at 800 °C for 5 min. Upon completion of the synthesis, we gently cooled the tube to room temperature under Ar gas flow by turning the heater off, and we obtained the MoS₂ layer on the SiO₂/Si substrate.

Device Fabrication. The details of the device fabrication process are provided in Figure S1 of the Supporting Information.

Device Packaging. We placed the Ez/MoS_2 array biosensor chip on a cavity package and bonded it *via* a wire bonding method. We subsequently placed the assembled array (PB-F87049, Kyocera) package into a chip carrier socket (8400, 3M) and connected it to external measurement equipment (semiconductor analysis system, Agilent 4156C).

Enzyme Film Immobilization. The 300 μ m thick SiO₂ substrate was first rinsed with acetone, isopropanol, and DI water. The rinsed SiO₂ substrate was cleaned with Piranha Clean using a solution of H_2SO_4/H_2O_2 (2:1 v/v) for 60 min. Subsequently, the substrate was carefully rinsed with DI water. After air-drying, O₂ plasma treatment of the surface of the SiO₂ substrate was performed for 2 min at P=18 W (COVANCE 1-MP, Femto) to create hydroxyl groups on it. Subsequently, we incubated the SiO₂ substrate in a 0.1 M APTES solution for 24 h. After rinsing the SiO₂ substrate, we incubated it in 1 mM p-LDH solution overnight. Then, the enzyme-immobilized SiO₂ (Ez-SiO₂) substrate was rinsed with DI water and was subsequently air-dried. Finally, the Ez-SiO₂ substrate was bonded to a PDMS chamber layer treated by an O₂ plasma machine at P=18 W for 2 min. The enzyme immobilization efficiency of this protocol was estimated to be ~12.8% from the data in the Supporting Information (Figure S11).

Enzyme Chamber/MoS₂ **Photodetector Integration.** We used a medical grade adhesive tape to bond the enzyme-film-coated SiO_2 substrate onto the Au electrode platforms on the optical reader substrate. Using alignment marks, we obtained an accurate alignment between each Ez chamber and the MoS_2 photoconductor channel. Finally, we created the integrated Ez/MoS_2 photoconductor architecture.

Experimental Setup and On-Chip Enzymatic Colorimetric **Analysis.** We used a semiconductor parameter analyzer (HP-4145B) to measure photocurrent variation of the MoS2 photodetector channels during the on-chip enzymatic colorimetric analysis. To achieve the on-chip enzymatic colorimetric analysis, we prepared a mixture of ferricytochrome c (1 mM) with the sample containing Dlactate. The high enzyme and substrate concentrations were used here to allow the sensitivity and response time of the biosensor to be only dependent on the analyte concentration. After loading the mixture in the EZ chamber, a laser emission at $\lambda = 450 \text{ nm} \pm 10\%$ and P = 0.5mW/cm² was illuminated onto the Ez chamber. The illumination wavelength was chosen because the absorption peak of the enzyme reaction lies near $\lambda = 450$ nm. The power density was measured using a conventional power and wavelength meter (OMM-6810B-100 V, Newport) (see Figure S3 in the Supporting Information). In this study, the linear normalization of a monochrome signal was performed according to the formula below:

$$I_{\mathrm{Norm}} = (I - I_{\mathrm{min}}) \frac{\mathrm{new} \, I_{\mathrm{max}} - \mathrm{new} \, I_{\mathrm{min}}}{I_{\mathrm{max}} - I_{\mathrm{min}}} + \mathrm{new} \, I_{\mathrm{min}}$$

where $I_{
m Norm}$, $I_{
m Max}$, $I_{
m min}$, new $I_{
m max}$ new $I_{
m min}$, and I are normalized, measured maximum, measured minimum, measured, normalized maximum, normalized minimum, and measured intensity, respectively.

Standard Artificial Saliva and Urine. We prepared artificial saliva by dissolving 5 mM NaCl, 1 mM CaCl₂, 15 mM KCl, 1 mM citric acid, 1.1 mM KSCN, and 4 mM NH₄Cl in distilled water. The pH of artificial saliva was adjusted to 6.7, which is the average pH of healthy human saliva. ^{49–51} We also purchased artificial urine from Carolina Biological Supply Company (Burlington, NC, USA).

Swine and Human Samples. To collect a swine sample, all the procedures were conducted in accordance with the National Institutes of Health (NIH) Guide for the Care and Use of Laboratory Animals (12) and were approved by the University Committee on Use and Care of Animals (UCUCA) at the University of Michigan (Protocol No. 00005009). Blood samples were drawn from a healthy donor after obtaining informed consent according to an Institutional Review Board (IRB)-approved protocol. All the specimens were collected in ethylenediaminetetraacetic acid tubes and were processed to obtain plasma and serum within 3 h. All human clinical samples tested were deidentified of all Protected Health Information (PHI).

Sample Preparation Procedure. As the first step, we prepared homogeneous matrixes. Prior to the spiking process, we confirmed that D-lactate did not exist at a significant level of concentration in the matrixes by testing them with our biosensor and a spectrometer. As such, these matrixes served as blank solutions in our tests. Subsequently, we diluted 10 μ L of a 100 mM D-lactate standard solution with 990 μ L of PBS to prepare a 1 mM standard solution. By diluting 10 μ L of the 1 mM D-lactate solution with 90 μ L of PBS, we next obtained a 100 μ L standard solution. Repeating these dilution steps, we obtained D-lactate solutions at 10^3 , 10^2 , 10^1 , 10^0 , 10^{-1} , 10^{-2} , 10^{-3} , and $10^{-4} \mu g/mL$. Then, we spiked the matrixes above with 10 μL of those standard solutions to prepare testing samples. To ensure high statistical confidence, we repeated these steps five times for each sample. Prior to the test, we prepared a mixture of the spiked sample and the D-lactate substrate with a 96% and 4% volume ratio, and we loaded the mixture into the detection chamber of the biosensor. In addition, for the preclinical samples of saliva, urine, and serums, we diluted 50% with PBS solution before loading them onto the device.

Fabrication of MoS₂ with Varying Thickness. Using a thermal release tape, we transferred MoS₂ flakes from a natural bulk MoS₂ ingot (purchased from SPI, Inc.) onto a substrate with a pressure applied to the tape using a rubber roll. Varying the pressure allowed us to vary the number of layers in the MoS₂ flakes. The thicknesses of these MoS₂ flakes were visually identified from their surface color contrast observed using an optical microscope and quantitatively measured using AFM. The fabrication of photodetectors using these MoS₂ flakes followed the same lithographical patterning and etching methods in Figure S1.

Thickness Effect on MoS₂ Photodetectors' Optoelectronic Performance. We used a semiconductor parameter analyzer (Keithley 4200A-SCS) equipped with two ultrafast I-V modules (model: 4225-PMU) to perform optoelectronic characterizations. Photoresponse properties were recorded with the 450 nm laser light source (power density: 0.43 mW). To measure the low-frequency (0.1–10 Hz) noise fluctuations in the photocurrent signals, time-dependent photocurrent measurements $(I_{\rm ph}-t)$ were carried out by a voltage-retention mode with a time resolution of 20 ms, recording time of 1 min, and $V_{\rm ds}=0.4$ V with no gate bias applied to the photodetectors. Noise equivalent power was calculated by the time-dependent photocurrent data using the fast Fourier transform algorithm.

ASSOCIATED CONTENT

Supporting Information

The Supporting Information is available free of charge at https://pubs.acs.org/doi/10.1021/acsnano.1c01394.

Figures of Ez/MoS₂ optoelectronic biosensor fabrication process; AFM images and measured thicknesses of the 4 × 4 MoS₂ channel arrays; device design and setup for highly sensitive and rapid D-lactate detection with MoS₂ photodetector arrays; photoresponsivity of $4 \times 4 \text{ MoS}_2$ photodetector arrays; long-term stability and reproducibility of MoS2 photodetector photoresponse; chemical reaction pathway of D-lactate oxidation; absorbance spectrum of PBS solution with D-lactate oxidized by enzyme reaction; dynamic photocurrent profile of pixel #7 MoS₂ photodetector; photocurrent variations as a function of air gap between EZ chamber and MoS2 photodetector; stability of Ez/MoS2 optoelectronic biosensor and enzymatic activity over time; absorbance spectra of conjugated and unconjugated enzyme solutions; comparison of photoresponsivity of MoS₂ photodetectors; references (PDF)

AUTHOR INFORMATION

Corresponding Authors

Younggeun Park — Department of Mechanical Engineering and Michigan Center for Integrative Research in Critical Care, University of Michigan, Ann Arbor, Michigan 48109, United States; orcid.org/0000-0002-8346-6142; Email: ygpark@umich.edu

Xiaogan Liang — Department of Mechanical Engineering and Michigan Center for Integrative Research in Critical Care, University of Michigan, Ann Arbor, Michigan 48109, United States; ◎ orcid.org/0000-0002-7390-9130; Email: xiaoganl@umich.edu

Katsuo Kurabayashi — Department of Mechanical Engineering, Michigan Center for Integrative Research in Critical Care, and Department of Electrical Engineering and Computer Science, University of Michigan, Ann Arbor, Michigan 48109, United States; orcid.org/0000-0002-9613-3590; Email: katsuo@umich.edu

Authors

Byunghoon Ryu — Department of Mechanical Engineering, University of Michigan, Ann Arbor, Michigan 48109, United States; Occid.org/0000-0003-3654-6198

Seung Jun Ki — Department of Mechanical Engineering, University of Michigan, Ann Arbor, Michigan 48109, United States

Brendan McCracken – Michigan Center for Integrative Research in Critical Care, University of Michigan, Ann Arbor, Michigan 48109, United States

Amanda Pennington – Michigan Center for Integrative Research in Critical Care, University of Michigan, Ann Arbor, Michigan 48109, United States

Kevin R. Ward — Michigan Center for Integrative Research in Critical Care and Department of Biomedical Engineering, University of Michigan, Ann Arbor, Michigan 48109, United States; Department of Emergency Medicine, University of Michigan Medical School, Ann Arbor, Michigan 48109, United States

Complete contact information is available at: https://pubs.acs.org/10.1021/acsnano.1c01394

Author Contributions

⁺Y.P. and B.R. contributed equally to this work.

Author Contributions

Y.P., B.R., K.W., X.L., and K.K. conceived and designed the experiments. Y.P. performed integration of bio-optoelectronic structure. B.R. and S.K. performed MoS₂ conducting nanosheet fabrication and packaging. Y.P., B.R., and S.K. conducted optical property analysis, Raman spectroscopy, AFM, optoelectric characterization, and detection test. B.M. and A.P. carried out animal and human sample preparation, respectively. Y.P., B.R., and S.K. conducted the data analysis. X.L. and K.K. supervised the entire project. Y.P., B.R., S.K., X.L., and K.K. wrote the manuscript. All listed authors discussed the results and commented on this work. Y.P. and B.R. contributed equally.

Notes

The authors declare no competing financial interest.

ACKNOWLEDGMENTS

This work was supported by the National Science Foundation, NSF-ECCS program (1708706), NSF-CBET program (2030551), and Academic Research Fund and Mcubed (U064088) at the University of Michigan. The authors thank Drs. Stinger, McHugh, and Dickson for providing the clinical samples and Mr. Nguyen and Ms. Hartmann for assisting with the experiments.

REFERENCES

- (1) Mamas, M.; Dunn, W. B.; Neyses, L.; Goodacre, R. The Role of Metabolites and Metabolomics in Clinically Applicable Biomarkers of Disease. *Arch. Toxicol.* **2011**, *85* (1), 5–17.
- (2) Bamji-Stocke, S.; van Berkel, V.; Miller, D. M.; Frieboes, H. B. A Review of Metabolism-Associated Biomarkers in Lung Cancer Diagnosis and Treatment. *Metabolomics* **2018**, *14* (6), 81.
- (3) Calderón-Santiago, M.; Priego-Capote, F.; Turck, N.; Robin, X.; Jurado-Gámez, B.; Sanchez, J. C.; Luque de Castro, M. D. Human Sweat Metabolomics for Lung Cancer Screening. *Anal. Bioanal. Chem.* **2015**, *407* (18), 5381–92.
- (4) Delgado-Povedano, M. d. M.; Calderón-Santiago, M.; Priego-Capote, F.; Jurado-Gámez, B.; Luque de Castro, M. D. Recent Advances in Human Sweat Metabolomics for Lung Cancer Screening. *Metabolomics* **2016**, *12* (11), 166.
- (5) Cameron, S. J. S.; Lewis, K. E.; Beckmann, M.; Allison, G. G.; Ghosal, R.; Lewis, P. D.; Mur, L. A. J. The Metabolomic Detection of Lung Cancer Biomarkers in Sputum. *Lung Cancer* **2016**, *94*, 88–95.
- (6) Zorofchian, S.; Iqbal, F.; Rao, M.; Aung, P. P.; Esquenazi, Y.; Ballester, L. Y. Circulating Tumour DNA, MicroRNA and Metabolites in Cerebrospinal Fluid as Biomarkers for Central Nervous System Malignancies. *J. Clin. Pathol.* **2019**, 72 (4), 271–280.
- (7) Bianchetti, D.; Amelio, G. S.; Lava, S. A. G.; Bianchetti, M. G.; Simonetti, G. D.; Agostoni, C.; Fossali, E. F.; Milani, G. P. D-Lactic Acidosis in Humans: Systematic Literature Review. *Pediatr. Nephrol.* (Berlin) 2018, 33 (4), 673–681.
- (8) Kang, K. P.; Lee, S.; Kang, S. K. D-Lactic Acidosis in Humans: Review of Update. *Electrolyte Blood Pressure* **2006**, 4 (1), 53–56.
- (9) Levy, B. Lactate and Shock State: The Metabolic Riew. Current Opinion in Critical Care 2006, 12 (4), 315-321.
- (10) Marty, P.; Roquilly, A.; Vallée, F.; Luzi, A.; Ferré, F.; Fourcade, O.; Asehnoune, K.; Minville, V. Lactate Clearance for Death Prediction in Severe Sepsis or Septic Shock Patients during the First 24 h in Intensive Care Unit: An Observational Study. *Ann. Intensive Care* **2013**, 3 (1), 3.
- (11) Nielsen, C.; Kirkegård, J.; Erlandsen, E. J.; Lindholt, J. S.; Mortensen, F. V. D-Lactate Is a Valid Biomarker of Intestinal Ischemia Induced by Abdominal Compartment Syndrome. *J. Surg. Res.* **2015**, *194* (2), 400–404.

- (12) Ewaschuk, J. B.; Naylor, J. M.; Zello, G. A. D-Lactate in Human and Ruminant Metabolism. *J. Nutr.* **2005**, *135* (7), *1619*–*1625*.
- (13) Lei, G.; Zhang, J.; Wang, X.; Chen, M. Plasma D-Lactate Levels in Necrotizing Enterocolitis in Premature Infants. *Iran J. Pediatr* **2016**, 26 (2), No. e4403.
- (14) Lippi, G.; Salvagno, G. L.; Montagnana, M.; Brocco, G.; Guidi, G. C. Influence of Hemolysis on Routine Clinical Chemistry Testing. *Clin. Chem. Lab. Med.* **2006**, 44 (3), 311–6.
- (15) Gladden, L. B. Lactate Metabolism: A New Paradigm for the Third Millennium. *I. Physiol.* **2004**, *558*, 5–30.
- (16) Koukourakis, M. I.; Giatromanolaki, A.; Harris, A. L.; Sivridis, E. Comparison of Metabolic Pathways between Cancer Cells and Stromal Cells in Colorectal Carcinomas: A Metabolic Survival Role for Tumor-Associated Stroma. *Cancer Res.* **2006**, *66* (2), 632–637.
- (17) Talasniemi, J. P.; Pennanen, S.; Savolainen, H.; Niskanen, L.; Liesivuori, J. Analytical Investigation: Assay of D-Lactate in Diabetic Plasma and Urine. *Clin. Biochem.* **2008**, *41* (13), 1099–1103.
- (18) Favre, E.; Pugeaud, P.; Péringer, P. Automated HPLC Monitoring of Glucose, Glutamine, Lactate and Alanine on Suspended Mammalian Cell Reactors. *Biotechnol. Techniques* 1990, 4 (5), 315–320.
- (19) Galban, J.; de Marcos, S.; Castillo, J. R. Fluorometric-Enzymatic Lactate Determination Based on Enzyme Cytochrome B2 Fluorescence. *Anal. Chem.* **1993**, *65* (21), 3076–3080.
- (20) Soares, D. P.; Law, M. Magnetic Resonance Spectroscopy of the Brain: Review of Metabolites and Clinical Applications. *Clin. Radiol.* **2009**, *64* (1), 12–21.
- (21) Heinemann, B. A Rapid Colorimetric Method for the Determination of Lactic Acid in Milk. *J. Dairy Sci.* **1940**, 23 (10), 969–972.
- (22) Wu, F.; Huang, Y.; Huang, C. Chemiluminescence Biosensor System for Lactic Acid Using Natural Animal Tissue as Recognition Element. *Biosens. Bioelectron.* **2005**, *21* (3), 518–522.
- (23) Bernaudat, F.; Bülow, L. Rapid Evaluation of Nickel Binding Properties of His-Tagged Lactate Dehydrogenases Using Surface Plasmon Resonance. *Journal of Chromatography A* **2005**, *1066* (1), 219–224.
- (24) Hirakoba, K.; Yunoki, T. Blood Lactate Changes during Isocapnic Buffering in Sprinters and Long Distance Runners. *Journal of Physiological Anthropology and Applied Human Science* **2002**, 21 (3), 143–149.
- (25) Wang, Y.; Vaidyanathan, R.; Shiddiky, M. J. A.; Trau, M. Enabling Rapid and Specific Surface-Enhanced Raman Scattering Immunoassay Using Nanoscaled Surface Shear Forces. *ACS Nano* **2015**, *9* (6), 6354–6362.
- (26) Shah, N. C.; Lyandres, O.; Walsh, J. T.; Glucksberg, M. R.; Van Duyne, R. P. Lactate and Sequential Lactate-Glucose Sensing Using Surface-Enhanced Raman Spectroscopy. *Anal. Chem.* **2007**, *79* (18), 6927–6932.
- (27) Guo, L.; Xu, S.; Ma, X.; Qiu, B.; Lin, Z.; Chen, G. Dual-Color Plasmonic Enzyme-Linked Immunosorbent Assay Based on Enzyme-Mediated Etching of Au Nanoparticles. *Sci. Rep.* **2016**, *6* (1), 32755.
- (28) de la Rica, R.; Stevens, M. M. Plasmonic ELISA for the Ultrasensitive Detection of Disease Biomarkers with the Naked Eye. *Nat. Nanotechnol.* **2012**, *7* (12), 821–824.
- (29) de la Rica, R.; Stevens, M. M. Plasmonic ELISA for the Detection of Analytes at Ultralow Concentrations with the Naked Eye. *Nat. Protoc.* **2013**, 8 (9), 1759–1764.
- (30) Fuhrer, M. S.; Hone, J. Measurement of Mobility in Dual-Gated MoS₂ Transistors. *Nat. Nanotechnol.* **2013**, 8 (3), 146–147.
- (31) Ghatak, S.; Pal, A. N.; Ghosh, A. Nature of Electronic States in Atomically Thin MoS₂ Field-Effect Transistors. *ACS Nano* **2011**, *5* (10), 7707–7712.
- (32) Radisavljevic, B.; Radenovic, A.; Brivio, J.; Giacometti, V.; Kis, A. Single-Layer MoS₂ Transistors. *Nat. Nanotechnol.* **2011**, 6 (3), 147–150.
- (33) Tsai, D.-S.; Liu, K.-K.; Lien, D.-H.; Tsai, M.-L.; Kang, C.-F.; Lin, C.-A.; Li, L.-J.; He, J.-H. Few-Layer MoS₂ with High Broadband

- Photogain and Fast Optical Switching for Use in Harsh Environments. ACS Nano 2013, 7 (5), 3905–3911.
- (34) Xiao, D.; Liu, G.-B.; Feng, W.; Xu, X.; Yao, W. Coupled Spin and Valley Physics in Monolayers of MoS₂ and Other Group-VI Dichalcogenides. *Phys. Rev. Lett.* **2012**, *108* (19), 196802.
- (35) Lopez-Sanchez, O.; Lembke, D.; Kayci, M.; Radenovic, A.; Kis, A. Ultrasensitive Photodetectors Based on Monolayer MoS₂. *Nat. Nanotechnol.* **2013**, *8* (7), 497–501.
- (36) Park, Y.; Ryu, B.; Oh, B.-R.; Song, Y.; Liang, X.; Kurabayashi, K. Biotunable Nanoplasmonic Filter on Few-Layer MoS_2 for Rapid and Highly Sensitive Cytokine Optoelectronic Immunosensing. *ACS Nano* **2017**, *11* (6), 5697–5705.
- (37) Park, Y.; Ryu, B.; Deng, Q.; Pan, B.; Song, Y.; Tian, Y.; Alam, H. B.; Li, Y.; Liang, X.; Kurabayashi, K. An Integrated Plasmo-Photoelectronic Nanostructure Biosensor Detects an Infection Biomarker Accompanying Cell Death in Neutrophils. *Small* **2020**, *16* (1), 1905611.
- (38) Ryu, B.; Nam, H.; Oh, B.-R.; Song, Y.; Chen, P.; Park, Y.; Wan, W.; Kurabayashi, K.; Liang, X. Cyclewise Operation of Printed MoS₂ Transistor Biosensors for Rapid Biomolecule Quantification at Femtomolar Levels. *ACS Sensors* **2017**, *2* (2), 274–281.
- (39) Chen, J.; Chen, Z.; Boussaid, F.; Zhang, D.; Pan, X.; Zhao, H.; Bermak, A.; Tsui, C. Y.; Wang, X.; Fan, Z. Ultra-Low-Power Smart Electronic Nose System Based on Three-Dimensional Tin Oxide Nanotube Arrays. *ACS Nano* **2018**, *12* (6), 6079–6088.
- (40) Wi, S.; Kim, H.; Chen, M.; Nam, H.; Guo, L. J.; Meyhofer, E.; Liang, X. Enhancement of Photovoltaic Response in Multilayer MoS_2 Induced by Plasma Doping. *ACS Nano* **2014**, 8 (5), 5270–5281.
- (41) Chhowalla, M.; Shin, H. S.; Eda, G.; Li, L.-J.; Loh, K. P.; Zhang, H. The Chemistry of Two-Dimensional Layered Transition Metal Dichalcogenide Nanosheets. *Nat. Chem.* **2013**, *5* (4), 263–275.
- (42) Lee, Y.-H.; Zhang, X.-Q.; Zhang, W.; Chang, M.-T.; Lin, C.-T.; Chang, K.-D.; Yu, Y.-C.; Wang, J. T.-W.; Chang, C.-S.; Li, L.-J.; Lin, T.-W. Synthesis of Large-Area MoS₂ Atomic Layers with Chemical Vapor Deposition. *Adv. Mater.* **2012**, 24 (17), 2320–2325.
- (43) Li, H.; Zhang, Q.; Yap, C. C. R.; Tay, B. K.; Edwin, T. H. T.; Olivier, A.; Baillargeat, D. From Bulk to Monolayer MoS₂: Evolution of Raman Scattering. *Adv. Funct. Mater.* **2012**, *22* (7), 1385–1390.
- (44) Chen, M.; Nam, H.; Wi, S.; Ji, L.; Ren, X.; Bian, L.; Lu, S.; Liang, X. Stable Few-Layer MoS₂ Rectifying Diodes Formed by Plasma-Assisted Doping. *Appl. Phys. Lett.* **2013**, *103* (14), 142110.
- (45) Scheuschner, N.; Ochedowski, O.; Kaulitz, A.-M.; Gillen, R.; Schleberger, M.; Maultzsch, J. Photoluminescence of Freestanding Single- and Few-Layer MoS₂. *Phys. Rev. B: Condens. Matter Mater. Phys.* **2014**, 89 (12), 125406.
- (46) Sung, H.-J.; Choe, D.-H.; Chang, K. J. The Effects of Surface Polarity and Dangling Bonds on the Electronic Properties of Monolayer and Bilayer MoS_2 on α -Quartz. New J. Phys. **2014**, 16 (11), 113055.
- (47) Gupta, S.; Shirodkar, S. N.; Kutana, A.; Yakobson, B. I. In Pursuit of 2D Materials for Maximum Optical Response. *ACS Nano* **2018**, *12* (11), 10880–10889.
- (48) Yue, X. F.; Wang, Y. Y.; Zhao, Y.; Jiang, J.; Yu, K.; Liang, Y.; Zhong, B.; Ren, S. T.; Gao, R. X.; Zou, M. Q. Measurement of Interfacial Thermal Conductance of Few-Layer MoS₂ Supported on Different Substrates Using Raman Spectroscopy. *J. Appl. Phys.* **2020**, 127 (10), 104301.
- (49) Kuksenkov, D. V.; Temkin, H.; Osinsky, A.; Gaska, R.; Khan, M. A. Low-Frequency Noise and Performance of GaN *p-n Junction* Photodetectors. *J. Appl. Phys.* **1998**, *83* (4), 2142–2146.
- (50) Shin, G. H.; Park, J.; Lee, K. J.; Lee, G.-B.; Jeon, H. B.; Choi, Y.-K.; Yu, K.; Choi, S.-Y. Si-MoS2 Vertical Heterojunction for a Photodetector with High Responsivity and Low Noise Equivalent Power. ACS Appl. Mater. Interfaces 2019, 11 (7), 7626–7634.
- (51) Rumyantsev, S. L.; Jiang, C.; Samnakay, R.; Shur, M. S.; Balandin, A. A. 1/f Noise Characteristics of MoS₂ Thin-Film Transistors: Comparison of Single and Multilayer Structures. *IEEE Electron Device Lett.* **2015**, 36 (5), 517–519.

- (52) Lin, M.-W.; Kravchenko, I. I.; Fowlkes, J.; Li, X.; Puretzky, A. A.; Rouleau, C. M.; Geohegan, D. B.; Xiao, K. Thickness-Dependent Charge Transport in Few-Layer MoS₂ Field-Effect Transistors. *Nanotechnology* **2016**, *27* (16), 165203.
- (53) Yang, J.; Wang, K.; Xu, H.; Yan, W.; Jin, Q.; Cui, D. Detection Platforms for Point-of-Care Testing Based on Colorimetric, Luminescent and Magnetic Assays: A Review. *Talanta* **2019**, 202, 96–110.
- (54) Cetin, A. E.; Coskun, A. F.; Galarreta, B. C.; Huang, M.; Herman, D.; Ozcan, A.; Altug, H. Handheld High-Throughput Plasmonic Biosensor Using Computational On-Chip Imaging. *Light: Sci. Appl.* **2014**, 3 (1), No. e122-e122.